

Dynamics and polarization of superparamagnetic chiral nanomotors in a rotating magnetic field

Konstantin I. Morozov¹ and Alexander M. Leshansky^{1,2*}

¹*Department of Chemical Engineering, Technion – Israel Institute of Technology, Haifa 32000, Israel and*

²*Technion Autonomous System Program (TASP), Haifa 32000, Israel*

Externally powered magnetic nanomotors are of particular interest due to the potential use for *in vivo* biomedical applications. Here we develop a theory for dynamics and polarization of recently fabricated superparamagnetic chiral nanomotors powered by a rotating magnetic field. We study in detail various experimentally observed regimes of the nanomotor dynamic orientation and propulsion and establish the dependence of these properties on polarization and geometry of the propellers. Based on the proposed theory we introduce a novel “steerability” parameter γ that can be used to rank polarizable nanomotors by their propulsive capability. The theoretical predictions of the nanomotor orientation and propulsion speed are in excellent agreement with available experimental results. Lastly, we apply slender-body approximation to estimate polarization anisotropy and orientation of the easy-axis of superparamagnetic helical propellers.

Introduction

The emergent interest in artificial “nature-inspired” micro- and nano-structures that can be remotely actuated, navigated and delivered to a specific location *in-vivo* is largely driven by the immense potential this technology offers to biomedical applications. Several approaches are currently of interest ranging from catalytically driven (chemical-fuel-driven) nanomotors to thermally, light and ultrasound-driven colloids (see [1] for state-of-the-art review of the subject). An alternative approach relies on externally powered nanomotors, where the particle is propelled through media by an external magnetic field. This allows contact-free and fuel-free propulsion in biologically active systems without chemical modification of the environment. In particular, it was shown [2–4] that a weak *rotating* magnetic field can be used efficiently to propel *chiral ferromagnetic nanomotors*. These nanohelices are magnetized by a strong magnetic field and retain remanent magnetization when stirred by a relatively weak (of the order of a few milli Tesla) rotating uniform magnetic field. The typical propulsion speeds offered by this technique are four-five orders of magnitude higher than these offered by the traditional techniques based on gradient of magnetic field, e.g. [5]. In the past few years the new technique has attracted considerable attention [6–9]. Various methods, such as “top-down” approach [3], glancing angle deposition [2] and direct laser writing (DLW) combined with vapor deposition [6], have been developed toward fabrication of ferromagnetic nanohelices. Experiments [7, 9] showed that at low frequency of the rotating

magnetic field nanomotors *tumble* in the plane of the field rotation without propulsion. However, upon increasing the field frequency, the tumbling switches to *wobbling* and the precession angle (between the axis of the field rotation and the helical axis) gradually diminishes and a corkscrew-like *propulsion* takes over.

Most recently an alternative method for micro-fabrication of *superparamagnetic* nanomotors was reported [10, 11]. The method relies on DLW and two-photon polymerization of a curable superparamagnetic polymer composite. These helices do not possess remanent magnetization, but are magnetized by the applied magnetic field. The advantages of using superparamagnetic polymer composite are the ease of microfabrication as magnetic material is already incorporated into the polymer (no need for thin film deposition), low toxicity [11] and the lack of magnetically-driven agglomeration of adjacent nanomotors in the absence of an applied field. Qualitatively, the dynamics of superparamagnetic helices resembles that of ferromagnetic nanomotors, i.e. they exhibit tumbling, wobbling and propulsion upon increasing frequency of the driving field. The magnetic properties of superparamagnetic nanohelices are characterized by their effective magnetic susceptibility and orientation of the magnetic *easy-axis*, generally dominated by the geometric effects [12]. Orientation of the easy-axis plays a central role in controlling the dynamics of superparamagnetic nanomotors in a way similar to orientation of the magnetic moment of permanently magnetized nanohelices. It was recently shown that orientation of the magnetic easy-axis in polymer composites can be manipulated in order to minimize tumbling/wobbling and maximize propulsion, by aligning (otherwise randomly dispersed) superparamagnetic nanoparticles prior to crosslinking the polymer matrix [13].

Physically, the dynamics of the magnetic nanomo-

*Electronic address: lisha@tx.technion.ac.il

tors is governed by the interplay of magnetic and viscous forces. Despite the high interest, the theory for the dynamics of magnetically driven nanomotors is quite limited. A recent study [14] addressed optimization of the chirality that maximizes the propulsion speed at a prescribed driving field assuming perfect alignment of the helix along the axis of the field rotation. In Refs. [15, 16] the hydrodynamic aspects of wobbling-to-swimming transition for a helix with purely transverse permanent magnetization were studied asymptotically and numerically showing a qualitative agreement with experiments. Ghosh et al. [9] found the formal mathematical solution for the orientation of permanently magnetized nanomotors. In [17] we studied in detail the dynamics of ferromagnetic chiral nanomotors and established the relation between their orientation and propulsion with the actuation frequency, remanent magnetization and the geometry. The theoretical predictions for the transition threshold between regimes and nanomotor alignment and propulsion speed in [17] showed excellent agreement with available experimental results.

No theoretical study concerning the dynamics of polarizable superparamagnetic nanomotors (e.g. in [10–13]) has been reported. In the present paper we propose an original theory for dynamics and polarization of superparamagnetic helical propellers and compare the predictions of the theory to previously reported experimental results.

Polarizable helix in rotating magnetic field: problem formulation

Let us consider the dynamics of polarizable helix in the external rotating magnetic field. We use two different coordinate frames – the laboratory coordinate system (LCS) fixed in space and the body-fixed coordinate system (BCS) attached to the helix (see Fig. 1). The coordinate axes of the two frames are XYZ and $x_1x_2x_3$, respectively. We denote by \mathbf{H} the externally imposed rotating (uniform) magnetic field. We also assume that in the LCS the field rotates in the XY -plane

$$\mathbf{H}^{LCS} = H(\cos \omega t, \sin \omega t, 0), \quad (1)$$

where H and ω are, correspondingly, the field amplitude and angular frequency.

Once the external field (1) is turned on, the helix polarizes. Owing to the magnetic anisotropy of the helix, the polarization vector \mathbf{M} is not generally aligned with \mathbf{H} . We assume uniaxial magnetic anisotropy of the helix with director \mathbf{n} . The general form of the uniaxial magnetic susceptibility tensor χ

is [18]

$$\chi_{ik} = \chi_0 \delta_{ik} + \Delta\chi(n_i n_k - \frac{1}{3} \delta_{ik}), \quad (2)$$

where χ_0 is the isotropic part of the magnetic susceptibility, δ_{ik} is the delta-symbol, $\Delta\chi = \chi_{\parallel} - \chi_{\perp}$ is the scalar parameter of magnetic anisotropy with χ_{\parallel} and χ_{\perp} being the main components of the tensor χ along the anisotropy axis and in the transverse direction, respectively. In this paper we assume *easy-axis anisotropy*, i.e., the positive values of parameter $\Delta\chi$. As we will see below, the case of an *easy-plane anisotropy* characterized by the negative values of $\Delta\chi$ is less relevant towards the present study since the helix cannot propel. We assume an arbitrary angle Φ between the director \mathbf{n} and the helical x_3 -axis. In the BCS \mathbf{n} can be written in the form

$$\mathbf{n}^{BCS} = (\sin \Phi, 0, \cos \Phi), \quad (3)$$

The orientation of the BCS with respect to the LCS is determined by three Euler angles φ , θ and ψ [22], as shown schematically in Fig. 1.

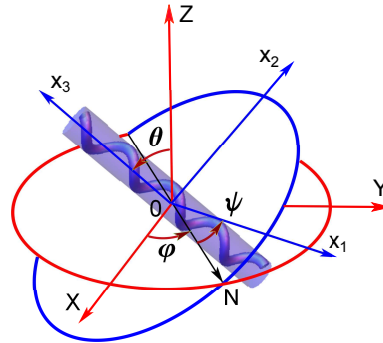


FIG. 1: The laboratory and body-fixed coordinate systems with the corresponding axes XYZ and $x_1x_2x_3$ and the definition of the Euler angles φ , θ and ψ . For simplicity, the cylindrical envelope of a helix is shown.

The rotational magnetic field (1) polarizes the helix producing the magnetic moment $\mathcal{M} = \mathbf{M}V = \chi \cdot \mathbf{H}V$ (with V being the helix volume), and also the magnetic torque $\mathbf{L}_m = \mathcal{M} \times \mathbf{H}$. Substituting the expression for susceptibility, we find that

$$\mathbf{L}_m = \Delta\chi H^2 V [\mathbf{n} \times \mathbf{h}] (\mathbf{n} \cdot \mathbf{h}), \quad (4)$$

where $\mathbf{h} = \mathbf{H}/H$ is the unit vector of the external field.

This torque is a source of both rotational and translational movements of the particle. In the Stokes approximation, the helix motion is governed by the balance of external and viscous forces and torques acting on the particle [19]

$$0 = \boldsymbol{\xi} \cdot \mathbf{U} + \mathcal{B} \cdot \boldsymbol{\Omega}, \quad (5)$$

$$\mathbf{L}_m = \mathcal{B}^T \cdot \mathbf{U} + \boldsymbol{\kappa} \cdot \boldsymbol{\Omega}, \quad (6)$$

where \mathbf{U} and $\mathbf{\Omega}$ are the translational and angular velocities of helix, $\boldsymbol{\xi}$, $\boldsymbol{\kappa}$ and \mathbf{B} are the translation, rotation and coupling viscous resistance tensors, respectively [19]. We have also assumed in Eq. (5) that no external force is exerted on the helix.

The formal solution of the problem can be readily obtained from Eqs. (5), (6):

$$\mathbf{U} = -\boldsymbol{\xi}^{-1} \cdot \mathbf{B} \cdot \mathbf{\Omega}, \quad \mathbf{\Omega} = \boldsymbol{\kappa}_{\text{eff}}^{-1} \cdot \mathbf{L}_m, \quad (7)$$

where $\boldsymbol{\kappa}_{\text{eff}} = \boldsymbol{\kappa} - \mathbf{B}^T \cdot \boldsymbol{\xi}^{-1} \cdot \mathbf{B}$ is the re-normalized viscous rotation tensor.

The problem of the helix dynamics can be decomposed into two separate problems: (i) rotational motion of an *achiral* slender particle i.e. with $\mathbf{B} = 0$ and diagonal $\boldsymbol{\kappa}$ with components $\kappa_{11} = \kappa_{22} = \kappa_{\perp} > \kappa_{33} = \kappa_{\parallel}$, e.g. axially symmetric slender particle, such as cylinder or prolate spheroid enclosing the helix (see Fig. 1), and (ii) translation of a *chiral* particle rotating with a prescribed angular velocity found in (i) (see [17] for detailed justification of such decomposition).

In the following sections we consider both problems.

Polarizable cylinder in a rotating magnetic field

It is convenient to right down the equation of the rotational motion (the second equation in Eqs. (7)) in the BCS in which the tensor $\boldsymbol{\kappa}$ takes a diagonal form [20]. The director \mathbf{h} of the magnetic field (1) in the BCS is $\mathbf{h}^{BCS} = \mathbf{R} \cdot \mathbf{h}$, where \mathbf{R} is the rotation matrix [21] (see Appendix A). Substituting components of the angular velocity $\mathbf{\Omega}$ [22] into the second equation in (7), the torque balance takes the form:

$$A(\mathbf{n} \cdot \mathbf{R} \cdot \mathbf{h})[\mathbf{n} \times (\mathbf{R} \cdot \mathbf{h})]_{x_1} = \dot{\varphi} s_{\theta} s_{\psi} + \dot{\theta} c_{\psi}, \quad (8)$$

$$A(\mathbf{n} \cdot \mathbf{R} \cdot \mathbf{h})[\mathbf{n} \times (\mathbf{R} \cdot \mathbf{h})]_{x_2} = \dot{\varphi} s_{\theta} c_{\psi} - \dot{\theta} s_{\psi}, \quad (9)$$

$$pA(\mathbf{n} \cdot \mathbf{R} \cdot \mathbf{h})[\mathbf{n} \times (\mathbf{R} \cdot \mathbf{h})]_{x_3} = \dot{\varphi} c_{\theta} + \dot{\psi}. \quad (10)$$

Here $A = \Delta\chi H^2 V / \kappa_{\perp}$ is the characteristic frequency of the problem. We also use here the compact notation throughout the paper, i.e. $s_{\psi} = \sin \psi$, $c_{\theta} = \cos \theta$, etc. and the dot stands for the time derivative. The rotational friction coefficient ratio $p = \kappa_{\perp} / \kappa_{\parallel} \gtrsim 1$ depends on the aspect ratio of the cylinder: it is $p \simeq 1$ for a short cylinder (i.e. disk), for which $\kappa_{\parallel} \simeq \kappa_{\perp}$ and increases with the growth of the aspect ratio [19].

Generally, overdamped dynamics of a magnetic particle in a rotating magnetic field can be realized via *synchronous* and *asynchronous* regimes [23, 24]. The synchronous regime is observed when there is a constant phase-lag between the Euler angle φ of the

particle body and the external magnetic field \mathbf{H} while the angles θ and ψ are not varying with time. As we show in the next section, the solution to the problem in the synchronous regime can be found analytically.

Synchronous regime: low-frequency tumbling solution

The low-frequency tumbling solution can be obtained by using the following ansatz for the Euler angles: $\psi = 0$, $\theta = \pi/2$, $\varphi = \omega t - \varphi_0$, where φ_0 is a constant. With these values, the components of unit vector \mathbf{h} in the BCS become

$$(\mathbf{R} \cdot \mathbf{h})_{x_1} = c_{\varphi_0}, \quad (\mathbf{R} \cdot \mathbf{h})_{x_2} = 0, \quad (\mathbf{R} \cdot \mathbf{h})_{x_3} = -s_{\varphi_0}. \quad (11)$$

As a result, Eqs. (8) and (10) are satisfied identically, whereas Eq. (9) determines the constant φ_0 :

$$A s_{2(\Phi - \varphi_0)} = 2\omega. \quad (12)$$

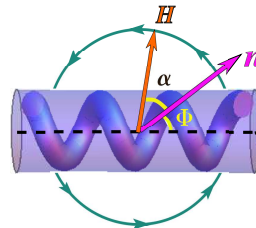


FIG. 2: The low-frequency synchronous regime. Both the helical axes and axes of magnetic anisotropy lie in the field rotation plane. The anisotropy axes \mathbf{n} inclined at an angle Φ to the helical axis. The rotating magnetic field outruns \mathbf{n} by the angle α .

The solution describes a *tumbling* regime, e.g., helix rotation about its short axis. The main feature of this regime is the fact that the easy-axis \mathbf{n} and the x_3 -axis of the cylinder both lie *in the field plane*, as shown in Fig. 2. Physically, this regime can be understood from the next qualitative argument. In the constant magnetic field, the helix magnetic moment \mathbf{M} and easy-axis \mathbf{n} are oriented along the field direction; the orientation of the x_3 -axis is arbitrary, while it forms a solid angle Φ with \mathbf{n} . In the weakly (quasi-statically) rotating magnetic field, \mathbf{M} and \mathbf{n} rotate with a small lag behind the external field \mathbf{H} . Thus, vectors \mathbf{M} and \mathbf{n} both prove to be in the plane of the field rotation. The degeneracy in the orientation of the propeller, however, is removed: the viscous friction causes the x_3 axis to align in the plane of the field rotation. The difference $\alpha = \Phi - \varphi_0$ in Eq. (12) determines the outrunning angle of the rotating field

\mathbf{H} relatively to the easy-axis \mathbf{n} (see Fig. 2). In the static magnetic field, $\omega = 0$, and both vectors coincide, i.e. $\alpha = 0$. As seen from Eq. (12), the solution exists within the limiting interval of field frequencies, from $\omega = 0$, up to the maximal value $\omega_I = A/2$. When $\omega = \omega_I$, the angle $\alpha = 45^\circ$ and the magnetic torque \mathbf{L}_m reaches its maximal value (see Eq. (4) and left-hand side of Eqs. (8) and (12)), i.e., a further increase of the field frequency leads to the breakdown of the synchronous rotation and transition to the asynchronous regime.

There is, however, an additional synchronous solution that branches from the tumbling solution one at the *finite value* of the driving frequency ω_* prior to transition to the asynchronous regime. The transition to this additional *high-frequency (wobbling) solution* can be expected by the following reasoning applicable for *slender (rod-like) particles*. The low-frequency tumbling solution illustrated in Fig. 2 is characterized by high viscous friction owing to the propeller rotation about its short axes. The rotation around the longer x_3 -axis would be accompanied by a significant reduction of the viscous friction, but at the same time, by higher value of magnetic energy $E_m = -(\mathbf{H} \cdot \boldsymbol{\chi} \cdot \mathbf{H})V/2$ [25]. Therefore, there is a *competition* between the magnetic and frictional torques. In the low-frequency tumbling regime, the viscous friction is of secondary importance – it is only responsible for removing the degeneracy of the propeller’s orientation, as any deviations from $\theta = 0$ (i.e. precession) are suppressed by the viscous torques acting to bring the x_3 -axis back to the plane of field rotation.

Upon increasing the driving frequency, ω , however, the role of the viscous forces increases and their interplay with the magnetic forces results into the new high-frequency wobbling regime.

Concluding this section, we point out that the higher the particle slenderness, the more pronounced is the competition between the magnetic and viscous forces. In contrast, in the case of disk-like platelets (see, e.g., Ref. [26]), the anisotropy of rotational friction coefficient is negligible, $p \approx 1$, and orientation of such platelets is determined solely by the magnetic forces. As a result, platelets rotate in such a way that the plane formed by their two major eigenvectors of the susceptibility tensor align with the plane of the rotating magnetic field for all field frequencies. There are also two potential cases with polarizable helices (with $p > 1$) where the competition between the magnetic and viscous forces cancels out. (i) The case of positive magnetic anisotropy, $\Delta\chi > 0$, when easy-axis \mathbf{n} is strictly perpendicular to the helix axis x_3 . This polarization is optimal for the helix propulsion: the magnetic field enforces the helix to spin around its

longer axis with minimal rotational friction, i.e. the tumbling is prevented for all driving frequencies. The recently fabricated superparamagnetic micro-helices with adjusted magnetic anisotropy in [13] possess this type of polarization. (ii) For the case of the easy-plane anisotropy, $\Delta\chi < 0$, the rotating magnetic field drives the helix to align its easy-plane with the plane of the field rotation. However, since both principal polarization axes in the easy-plane are equivalent, the lack of magnetic anisotropy in the field plane would yield no corkscrew-like rotation and propulsion.

Synchronous regime: High-frequency wobbling solution

The high-frequency wobbling solution can be found by using the following ansatz for the φ -Euler angle: $\varphi = \omega t$. Thus the projections of the unit vector \mathbf{h} in the BCS are

$$(\mathbf{R} \cdot \mathbf{h})_{x_1} = c_\psi, \quad (\mathbf{R} \cdot \mathbf{h})_{x_2} = -s_\psi, \quad (\mathbf{R} \cdot \mathbf{h})_{x_3} = 0. \quad (13)$$

The system of three equations (8)-(10) reduces to the following system of two equations governing the two remaining Euler angles, ψ and θ :

$$\omega_* c_\psi = \omega s_\theta, \quad (14)$$

$$-\gamma \omega_* s_{2\psi} = 2\omega c_\theta, \quad (15)$$

where we introduced the critical frequency $\omega_* = (A/2)s_{2\Phi}$ and the “steerability” parameter $\gamma = p \tan \Phi$ (see the Discussion Sec. for details). There is a non-trivial solution of (14-15) provided that $\gamma = p \tan \Phi \geq 1$,

$$c_\psi = \frac{(1 + \gamma^2)^{1/2}}{\gamma\sqrt{2}} \left(1 + \sqrt{1 - \omega^2/\omega_{II}^2} \right)^{1/2}, \quad (16)$$

$$s_\theta = \frac{\sqrt{2}}{(1 + \gamma^2)^{1/2}} \frac{\omega_{II}}{\omega} \left(1 + \sqrt{1 - \omega^2/\omega_{II}^2} \right)^{1/2}. \quad (17)$$

Here we used the notation

$$\omega_{II} = \omega_* \frac{1 + \gamma^2}{2\gamma} = \frac{\Delta\chi H^2 V}{\kappa_\perp} \frac{1 + \gamma^2}{4\gamma} \sin 2\Phi. \quad (18)$$

The high-frequency solution (16-17) branches from the low-frequency solution (12) at frequency $\omega = \omega_*$ where $\theta = \pi/2$ and persists in the limiting frequency interval $\omega \in [\omega_*, \omega_{II}]$.

The high-frequency solution corresponds to *wobbling* dynamics where the increase in driving frequency from ω_* up to ω_{II} yields the gradual decrease in the angle θ between the propeller’s x_3 -axis and

the Z -axis of the field rotation, or the precession angle. The minimal precession angle θ_{\min} is attained at $\omega = \omega_{\text{II}}$

$$(s_{\theta})_{\min} = \frac{\sqrt{2}}{(1 + \gamma^2)^{1/2}}. \quad (19)$$

The maximal frequency, ω_{II} , is usually termed as *step-out frequency* $\omega_{s-o} \equiv \omega_{\text{II}}$. At frequencies $\omega > \omega_{s-o}$ the high-frequency solution breaks down and the synchronous regime switches to the asynchronous one.

Finally, note that the high-frequency solution (16–17) requires $\gamma > 1$, i.e. helices that fail to fulfil this conditions would exhibit the low-frequency tumbling, i.e., non-propulsive dynamics followed by the asynchronous tumbling for frequencies $\omega > \omega_{\text{I}}$. Both regimes of tumbling motion take place *in plane* of the field rotation (see Fig. 2), they are characterized by a single angular variable α and have been studied in detail, e.g. see Refs. [23, 24].

Comparison to the experiment

Let us now compare the experimental results with our theoretical predictions. The experimental results [12] for the precession angle as a function of the frequency of the rotating magnetic field are depicted in the inset of Fig. 3. The data was obtained for three prototypes or ‘agents’ (shown here as squares, triangles, and circles), having similar characteristics, i.e. microhelices with 3 full turns, helical radius $R = 2.25 \mu\text{m}$, filament width $d = 1.8 \mu\text{m}$, helical angle $\Theta = 70^\circ$, fabricated from polymer composite with 2% (vol) superparamagnetic magnetite $\sim 11 \text{ nm}$ diameter nanoparticles. The empty and filled symbols correspond to two different strengths of the applied external field, equal to 3 mT and 6 mT, respectively. Since the magnetic and geometric properties of the helices are similar, their corresponding precession angles found at given field amplitude prove to be rather close. However, the reported step-out frequencies $\nu_{s-o} = \omega_{\text{II}}/2\pi$ exhibit some scattering, especially noticeable at higher value of the magnetic field, $H = 6 \text{ mT}$, with $\nu_{s-o} = 4 \text{ Hz}$, 4.6 Hz and 5.1 Hz .

As follows from Eq. (17), the precession angle is a function of the steerability parameter γ and the frequency ratio ν/ν_{s-o} . The re-scaled data shown in Fig. 3 falls on the master curve (17) with the single best-fitted parameter $\gamma = 9.3$. For $\gamma = 9.3$ we find that $\nu_*/\nu_{s-o} = 2\gamma/(1 + \gamma^2) = 0.21$. This prediction is also in an excellent agreement with the experimental values $\nu_*/\nu_{s-o} = 0.20, 0.22$ and 0.25 , found in Ref. [12] for the three prototypes. Let us next esti-

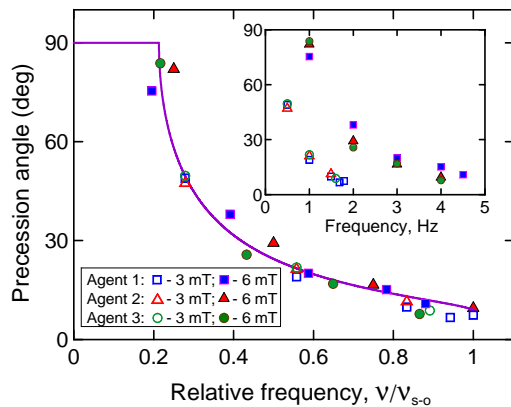


FIG. 3: Precession angle as a function of the frequency ratio ν/ν_{s-o} . The symbols stand for the experimental results of [12] for three prototypes. The empty and filled symbols correspond to the applied field of 3 mT and 6 mT, respectively. The solid line is the theoretical prediction by Eq. (17) with parameter $\gamma = 9.3$. The inset depicts the precession angle in [12] as a function of frequency ν (Hz).

mate the limiting (minimal) value of the precession angle, θ_{\min} , corresponding to the step-out frequency ν_{s-o} . Using Eq. (19) it is $\theta_{\min} = \arcsin \sqrt{2/(1 + \gamma^2)}$. For $\gamma = 9.3$ we find $\theta_{\min} = 8.7^\circ$ which is quite close to the experimental measurement $\theta_{\min} \approx 8^\circ$ [12].

Now the angle Φ between the easy vector \mathbf{n} and the axis x_3 of the helix corresponding to the best-fitted value of $\gamma = 9.3$ can be determined. From the definition of γ we have $\Phi = \arctan(\gamma/p)$, where $p = \kappa_{\perp}/\kappa_{\parallel}$. As done before in Ref. [17], we approximate the helix by the enclosing prolate spheroid and use the explicit expressions for κ_{\perp} and κ_{\parallel} available for ellipsoidal particles (see Appendix B). This ratio depends only on the aspect ratio a/b of the spheroid. For a 3-turn helix this ratio is $a/b \approx 3\pi/\tan\Theta$. For the helix angle $\Theta = 70^\circ$, we find $a/b \simeq 3.4$. The aspect ratio can be alternatively estimated using the micrograph of the helix given in Fig. 2 in Ref. [12]. The micrograph gives a slightly lower value, $a/b \approx 3$. Therefore, the corresponding values of the parameter $p = \kappa_{\perp}/\kappa_{\parallel}$ are 3.8 and 3.1, what finally determines the angle Φ of inclination of the easy-axis of magnetization \mathbf{n} to the helical x_3 -axis as $\Phi = 68 \div 72^\circ$. These estimates are confirmed by the rigorous particle-based calculations based on multipole expansion algorithm (see [17] for details). For example, for a helix with $\Theta = 70^\circ$ ($a/b \simeq 2.61$) we found $p \simeq 3.07$ resulting in $\Phi \simeq 71.7^\circ$. For a slightly less slender helix with $\Theta = 67^\circ$ (with $a/b \simeq 3.05$) we obtained $p \simeq 3.95$ yielding $\Phi \simeq 67^\circ$.

The propulsion velocity of the helical propeller along the axis of the field rotation, U_Z , can be determined from Eq. (7). Following the same arguments as

in [17], we assume helices with chirality along the x_3 -axis, i.e., that in the body-fixed coordinate frame the only non-zero component of \mathcal{B} is \mathcal{B}_\parallel . Thus, in the low-frequency tumbling regime we have $U_Z = 0$, whereas in the high-frequency regime it is $U_Z = -\omega c_\theta^2 \mathcal{B}_\parallel / \xi_\parallel$ (for details see [17]), where \mathcal{B}_\parallel and ξ_\parallel are the longitudinal (along the helix axes) components of the coupling and the translation viscous resistance tensors, respectively. Substituting the value of precession angle from Eq. (17) and normalizing the velocity with $R\omega_{s-o}$, with R being the helix radius, yields

$$\frac{U_Z}{R\omega_{s-o}} = \text{Ch} \frac{\omega}{\omega_{s-o}} \left[1 - \frac{2}{1 + \gamma^2} \frac{\omega_{s-o}^2}{\omega^2} \left(1 + \sqrt{1 - \frac{\omega^2}{\omega_{s-o}^2}} \right) \right], \quad (20)$$

where $\text{Ch} = -\mathcal{B}_\parallel / (\xi_\parallel R)$ is the chirality coefficient depending on the helix geometry only [17]. Thus, similarly to the precession angle, the propulsion velocity is a function of the helix geometry (via parameters γ and Ch) and the frequency ratio ν/ν_{s-o} .

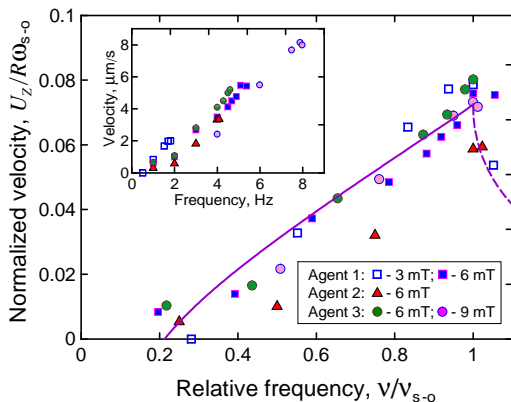


FIG. 4: Scaled propulsion velocity vs. frequency of the rotating magnetic field normalized by the step-out frequency. The experimental data (symbols) are from [12] for three different prototypes/agents. The solid line is the theoretical prediction by Eq. (20) with parameters $\gamma = 9.3$ and $\text{Ch} = 0.075$. The dotted line stands for the velocity in the asynchronous regime [17]. The inset shows the experimental results in dimensional form.

In the inset to Fig. 4, the experimental data [12] for the propulsion velocity as a function of the frequency of the rotating magnetic field is shown. The same symbol designations are used as in Fig. 3 and a new data for the applied field strength of 9 mT was added. As for the precession angle, the re-scaled data measured for three different values of the magnetic field collapse on the the master curve (20). The previously best-fitted value of $\gamma = 9.3$ and $\text{Ch} = 0.075$ are used. The data corresponding to the ‘agent’ #2 (Δ) shows a considerable deviation from the master curve, what might be a result of a slightly lower value of Ch .

To justify the parameter fitting, we computed Ch

numerically by the multipole expansion method described in [17]. Following [12], we take the 3-turn helix with $\Theta = 70^\circ$ and $R/r = 2.5$ (corresponding to $a/b \simeq 2.61$), where r stands for the filament radius. For such geometry we find $\text{Ch} = 0.056$. However for a slightly more slender helix with $\Theta = 67^\circ$ (corresponding to $a/b \approx 3.05$, which agrees with the micrograph in Fig. 2 in [12]), we obtain $\text{Ch} = 0.072$ in a very good agreement with the best-fitted value of 0.075.

Magnetic properties of helices

In this section we study the magnetic properties of helices. We assume that helices are superparamagnetic: they do not possess remanent spontaneous magnetization and become magnetized only in an external magnetic field. In practice, such helices are microfabricated by the solidification (photopolymerization) of a polymer matrix comprising the embedded superparamagnetic nanoparticles of typical size ~ 10 nm [11, 12]. The matrix crosslinking can take place both in the absence of external magnetic field [10, 11, 30] as well as with applied static homogeneous magnetic field [13]. In the former case the magnetic particles are randomly distributed (reference helices), whereas in the later case there is an anisotropic particle distribution (helices with adjusted anisotropy). Here we investigate the case of helices with *random* spatial distribution of superparamagnetic inclusions. Therefore, the magnetic susceptibility of the helix bulk material is an isotropic property characterized by the scalar parameter χ_0 determined by the values of concentration and magnetic moments of nanoparticles [28].

Our aim is determining the *effective* magnetic susceptibility χ of the helix as *a whole*. We define χ as the coefficient of proportionality between the helix magnetization $\mathbf{M} = \mathcal{M}/V$ (\mathcal{M} is magnetic moment of helix acquired in the external field magnetic field \mathbf{H} and V is the helix volume) and the value of this field: $\mathbf{M} = \chi \cdot \mathbf{H}$. Let us comment on this relation. Typically, magnetic susceptibility is defined as a coefficient of proportionality between magnetization \mathbf{M} and *internal* magnetic field \mathbf{H}_{in} . Internal magnetic field is a sum of the external field, \mathbf{H} , and the demagnetizing magnetic field, \mathbf{H}_d , owing to the magnetic material itself, $\mathbf{H}_{in} = \mathbf{H} + \mathbf{H}_d$ [25]. For magnetic particles the demagnetizing field \mathbf{H}_d depends on the body geometry, whereas the susceptibility χ is a property of a magnetic material only, i.e. geometry independent. For the helical geometry, the internal field \mathbf{H}_{in} proves to be fundamentally inhomogeneous one, and, therefore it is advantageous to characterize the apparent, or, effective susceptibility

of the helix as a whole with geometry dependent tensor χ . For sufficiently slender helices one can estimate the effective susceptibility tensor χ as a function of magnetic susceptibility χ_0 of the helix material and its geometry in the framework of slender body (SB) approximation.

Slender body approximation

The SB approximation assumes that locally a helical filament can be considered as a thin straight cylinder. We study the case of an *elliptical* cross-section of the filament with semi-axis \mathbf{a} having a fixed component along the helical axis and semi-axis \mathbf{b} oriented normally to the helical axis. Assumption of slenderness applies to helices with typical dimensions, i.e. the radius R and the pitch P , satisfying $R, P \gg \max(\mathbf{a}, \mathbf{b})$. In the experiments the helices are typically not slender (e.g. [12, 13, 30]), however, SB approximation allows the derivation of the closed-form formulae for the effective susceptibility and explains qualitatively the experimentally observed phenomena.

Here we consider two types of helices: *normal* helices with the cross-section elongated in the direction transverse to the helical axis ($\mathbf{b} > \mathbf{a}$), and *binormal* helices with longer cross-sectional axis having a fixed component along the helical axis ($\mathbf{a} > \mathbf{b}$). In what follows, we shall consider the normal helix.

In the body-fixed coordinate frame $x_1x_2x_3$ with the helix axis oriented along x_3 , the equation for the helix centerline can be written in the following parametric representation [27]

$$\mathbf{X}(s) = \left[\frac{\kappa}{\lambda^2} \cos(\lambda s), \frac{\kappa}{\lambda^2} \sin(\lambda s), \frac{\tau}{\lambda} s \right]. \quad (21)$$

Here s is the arc length and $\lambda = 1/\sqrt{R^2 + \frac{P^2}{4\pi^2}}$. Curvature κ and torsion τ are defined via helix radius R and pitch P as $\kappa = R\lambda^2$, $\tau = \frac{P}{2\pi}\lambda^2$.

Let $\{\mathbf{d}_1, \mathbf{d}_2, \mathbf{d}_3\}$ be the right-handed director basis defined at each position s along the axis of the filament [27]:

$$\begin{aligned} \mathbf{d}_1(s) &= \left[\frac{\tau}{\lambda} \sin(\lambda s), -\frac{\tau}{\lambda} \cos(\lambda s), \frac{\kappa}{\lambda} \right], \\ \mathbf{d}_2(s) &= [\cos(\lambda s), \sin(\lambda s), 0], \\ \mathbf{d}_3(s) &= \left[-\frac{\kappa}{\lambda} \sin(\lambda s), \frac{\kappa}{\lambda} \cos(\lambda s), \frac{\tau}{\lambda} \right]. \end{aligned} \quad (22)$$

$\mathbf{d}_3 = \partial\mathbf{X}(s)/\partial s$ is the vector tangent to the centreline of the filament. Vectors \mathbf{d}_1 (binormal) and \mathbf{d}_2 (normal) are assumed to be parallel, correspondingly, to the semi-axes of the filament cross-section (e.g. for

the normal helix \mathbf{d}_1 and \mathbf{d}_2 are parallel to the short and the long semi-axes, respectively).

The magnetic susceptibilities of a cylinder along the three principal axes read [25]

$$\chi_1 = \frac{\chi_0}{1 + 4\pi\chi_0N_1}, \chi_2 = \frac{\chi_0}{1 + 4\pi\chi_0N_2}, \chi_3 = \chi_0. \quad (23)$$

Here N_1 and $N_2 = 1 - N_1$ are the demagnetizing factors along the axis \mathbf{d}_1 and \mathbf{d}_2 , respectively, and we also assumed the zero value of the demagnetizing factor along the long axis of cylinder, $N_3 = 0$. The explicit expressions for demagnetizing factors are given in the Appendix C.

Eq. 23 indicates that in the applied magnetic field helical segments are polarized differently along the major axes: the easy direction is along the centerline, and the hard one is along the shorter cross-section. This property leads to the apparent anisotropy of magnetic susceptibility χ of the helix as a whole.

The SB approximation is the *local* theory: the magnetization of each segment is determined only by its geometry and by the applied magnetic field (see Eq. (2)). In other words, in the framework of SB approximation different parts of the helix do not interact, i.e. magnetize independently from each other. Therefore, the effective susceptibility χ of helix proves to be an additive property and can be determined by integration

$$\chi = L^{-1} \int_0^L (\chi_1 \mathbf{d}_1 \mathbf{d}_1 + \chi_2 \mathbf{d}_2 \mathbf{d}_2 + \chi_3 \mathbf{d}_3 \mathbf{d}_3) ds, \quad (24)$$

where L is the helix length along the centerline.

Let us denote the eigenvalues of matrix χ in the ascending order as $\chi_I \leq \chi_{II} \leq \chi_{III}$. Generally, all three eigenvalues are different and helix possesses biaxial magnetization. However, for the *integer* number of turns in the framework of SB approximation, the susceptibility tensor becomes *uniaxial*: two out of three eigenvalues coincide. In present study we shall consider this simple and practically relevant situation. The direct integration in Eq. (24) using Eqs. (23)-(22) demonstrates that the eigenvectors of χ are aligned with the BCS axes $x_1x_2x_3$; the magnetic anisotropy parameter $\Delta\chi$, defined as the difference of eigenvalues along the anisotropy (i.e. helical) axes and in transverse direction, $\Delta\chi = \chi_{\parallel} - \chi_{\perp}$, reads

$$\Delta\chi = \frac{1}{2}[(\chi_3 - \chi_1)(3 \cos^2 \Theta - 1) + \chi_1 - \chi_2]. \quad (25)$$

Particularly simple form of magnetic anisotropy parameter can be obtained for the case when $4\pi\chi_0 \ll 1$. The polymer composite used for nanomotor fabrication in Ref. [10, 11, 30] satisfies this condition. Indeed, taking the volume fraction of superparamagnetic inclusions $\phi = 0.02$, their mean diameter

$d_p = 11$ nm [11] and the saturation magnetization of the magnetite $M_s = 281$ Gs [30], at $T = 300$ K we can estimate that $4\pi\chi_0 = (2\pi^2/9)\phi M_s^2 d_p^3 / (k_B T) \approx 0.1$ [28]. Then taking the asymptotic small- χ_0 limit of susceptibilities in Eq. (23), $\Delta\chi$ in Eq. (25) can be further simplified into

$$\frac{\Delta\chi}{2\pi\chi_0^2} = N_1(3\cos^2\Theta - 1) + 1 - 2N_1. \quad (26)$$

The analogous result for the binormal helix is readily obtained from Eqs. (25) and (26) by interchanging indices $1 \leftrightarrow 2$.

The obtained result (26) indicates that magnetically, integer-number-of-turns helix is equivalent to a polarized spheroid with its polarization/easy-axis aligned along the helical x_3 -axis. The slender helices with a small pitch angle $\Theta < \Theta_*$ are characterized by the positive value of the anisotropy parameter $\Delta\chi$ (i.e. equivalent to prolate spheroid), whereas for the tight helices with high values of $\Theta > \Theta_*$ the anisotropy parameter becomes negative (i.e. equivalent to oblate spheroid or disk). The critical helix angle Θ_* at which $\Delta\chi$ changes sign is found from the relation $\cos^2\Theta_* = 1 - 1/(3N_1)$. It is depicted in the

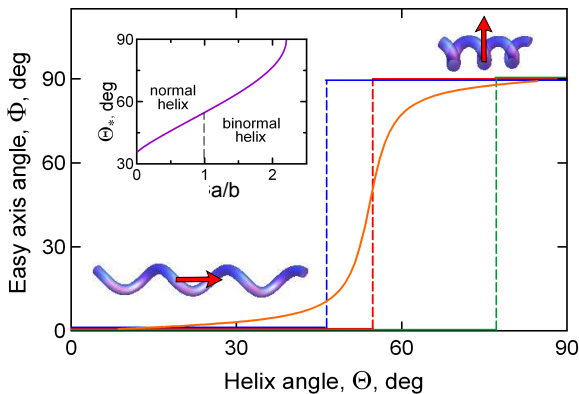


FIG. 5: Inclination angle Φ of the easy-axis as a function of the helix angle Θ for regular (red), normal (blue) and binormal (green) helices with integer number of turns. The aspect ratio of the filament cross-section for normal and binormal helices is $a/b = 2$. The orange curve corresponding to a regular helix with 3.3 full turns illustrates the effect of imperfectness on Φ (see details in the text); the helices and corresponding arrows illustrate the orientation of the easy-axis depending on the pitch angle Θ . The inset depicts the critical helix angle Θ_* vs. the filament cross-section aspect ratio a/b .

inset to Fig. 5 as a function of the aspect ratio a/b of the filament cross-section. For regular helix with a circular cross-section ($a = b$) we have $\Theta_*^r = 54.7^\circ$. The values of the critical angle Θ_* for the normal and binormal helices prove to be *strongly asymmetric* relatively to its value for regular helix. For example,

for $a/b = 2$, $\Theta_*^n = 45.8^\circ$ and $\Theta_*^{bn} = 76.6^\circ$ for the normal and binormal helices, respectively. The minimal value of this critical angle for the normal helix with infinitely thin filament cross-section ($a/b \rightarrow 0$) is $\Theta_*^n = 35.3^\circ$, whereas for the binormal helix it reaches its maximal value $\Theta_*^{bn} = 90^\circ$ already for aspect ratio $a/b \simeq 2.2$. The angle Φ formed by the main eigenvector (corresponding to the maximal eigenvalue χ_{III}) of the susceptibility tensor and the helix axes is depicted in Fig. 5 as a function of the helix angle Θ for regular (red), normal (blue) and binormal (green) helices. As seen, all dependencies are *step-like* functions: $\Phi = \mathcal{H}(\Theta - \Theta_*)$, where $\mathcal{H}(x)$ is the Heaviside function. This idealized solution is due to three simplifying assumptions: (i) local magnetization, (ii) integer number of helical turns and (iii) homogeneity of the geometrical and magnetic properties of helices. Any violation of (i)–(iii) or *imperfectness* should lead to deviation from the ideal dependence and to smoothing out of the step-like profile as illustrated in Fig. 5 by the orange line corresponding to a helix with non-integer number of turns. The detailed analysis of magnetization of polarizable helices requires numerical computations that are beyond the scope of the present study and will be considered elsewhere.

The idealized SB approximation allows to understand qualitatively the difference in the dynamics of slender ($\Theta < \Theta_*$) and tight ($\Theta > \Theta_*$) helices. In the former case, the easy-axis inclination angle $\Phi = 0$ so that the condition $p \tan \Phi > 1$ (obligatory for transition to wobbling, see the details above) is violated. That means that helices with pitch angles $\Theta < \Theta_*$ would only tumble and not propel. In contrast, for $\Theta > \Theta_*$, the inclination angle is at maximum, $\Phi = 90^\circ$, i.e. the optimal orientation for propulsion. These findings are in accord with recent experimental observations in [12], where helices with pitch angles $\Theta = 40^\circ, 50^\circ$ and 60° showed tumbling for any driving frequencies, while only the helices with the pitch angle $\Theta = 70^\circ$ exhibited corkscrew-like propulsion. We should mention, however, that within the SB approximation framework, the anisotropy is always uniaxial, meaning that tight helices possess easy-plane of magnetization (disk-like polarization with $\Delta\chi < 0$), while effective propulsion requires, besides alignment along the axis of field rotation (i.e. $\Phi \sim 90^\circ$) also magnetic anisotropy in the transverse plane. We anticipate that aforementioned imperfectness should yield deviation from the uniaxial anisotropy, e.g. two distinct non-zero anisotropy parameters, $\Delta\chi_1 = \chi_{III} - \chi_I$ and $\Delta\chi_2 = \chi_{II} - \chi_I$.

Discussion and concluding remarks

We developed the theory for dynamics and polarization of superparamagnetic chiral nanomotors powered by a rotating magnetic field. Depending on their geometry, magnetic properties and the parameters of actuating magnetic field (i.e. frequency and amplitude), the nanomotors are involved into synchronous motion (tumbling or wobbling) or twirl asynchronously. The effective nanomotor propulsion is enabled as a combined effect of two different factors. First factor is the “steerability” of the nanomotor, i.e. its ability to undergo synchronous precessive motion and propulsion. Mathematically, steerability can be characterized by the parameter $\gamma = p \tan \Phi$ that depends on both geometric and magnetic properties of the nanomotor. The nanomotors with $\gamma < 1$ are not propulsive and undergo tumbling for all driving frequencies, while $\gamma > 1$ controls the critical frequency of tumbling-to-wobbling transition, $\omega_* = (A/2) \sin 2\Phi$ and the minimal value of the wobbling angle $\theta_{min} \sim \gamma^{-1}$ (see Eq. 19). Increasing the slenderness of the propeller (i.e. increasing $p = \kappa_{\perp}/\kappa_{\parallel}$) and/or the inclination of the easy-axis of magnetic anisotropy relatively to the helix axis Φ , results in narrowing of the interval of tumbling frequencies, $[0, \omega_*]$ and better alignment via lowering of θ_{min} , i.e. improved steerability. The maximal steerability is attained as $\gamma \rightarrow \infty$ when the easy-axis is oriented transverse to the helix axis, i.e. $\Phi \approx 90^\circ$. In this case the propulsion is tumbling- and wobbling-free as the nanomotor aligns parallel to the axis of the field rotation for all frequencies. This situation corresponds to, e.g., nanohelices with “adjusted” easy-axis anisotropy [13].

The second factor is the anisotropy parameter of the effective susceptibility in the plane of field rotation, $\Delta\chi_{\perp}$. This anisotropy parameter defines the maximal value of the step-out frequency $\omega_{s-o} = \Delta\chi_{\perp} H^2 V / 2\kappa_{\parallel}$ at the best possible orientation, $\Phi \rightarrow \pi/2$ (see Eq. 18). In the synchronous wobbling regime the propulsion is *geometric*, as as the swimming speed $U_Z \approx \text{Ch} R \omega$ for sufficiently large γ (see Eq. (20)), i.e. it is the same for all values of $\Delta\chi_{\perp} \neq 0$. The step-out frequency, however, determines the upper limit for the propulsion speed, $U_{Zmax} = \text{Ch} \omega_{s-o} R$.

The predictions of our theory for the dynamic orientation and propulsion speed are in excellent agreement with available experimental results (see Figs. 3–4). Note that γ could not be estimated directly from the experiments in [12] since the easy-axis orientation, i.e. Φ , was not reported, and it was treated as fitting parameter. The chirality coefficient, Ch, determined self-consistently agrees with the corresponding estimated experimental value.

The developed slender body (SB) theory provides a qualitative description of the effective polarization of the nanomotors. In particular, it predicts the uniaxial magnetic anisotropy of helices with integer number of turns. Orientation of the easy-axis is a step-function of the helix pitch angle, i.e. slender helices possess an easy-axis aligned along the helical axis ($\Phi = 0$, $\Delta\chi > 0$), while tight helices possess (disk-like) easy-plane anisotropy ($\Phi = 90^\circ$, $\Delta\chi < 0$). Thus, within the SB approximation framework slender helices are not steerable ($\gamma = 0$), while tight helices are shown to be optimally oriented for propulsion by the rotating field in agreement with experimental observations [12]. However, it is impossible to estimate the propulsion velocity of the tight helices in the SB framework, as $\Delta\chi_{\perp} = 0$ due to magnetization isotropy in the transverse plane. In practice, however, transverse magnetization of nanomotors with non-adjusted easy-axis is anisotropic owing to potential shape effects, non-slenderness, fluctuations in the spatial distribution of superparamagnetic inclusions, etc. In [13] non-adjusted helices exhibited nearly optimal orientation, $\Phi \approx 90^\circ$, while the propulsion velocity of adjusted and non-adjusted helices under similar conditions felt on the same straight line when plotted vs. driving frequency in accord with our arguments above. The difference in the step-out frequency, $\nu_{s-o} \approx 5$ Hz and $\nu_{s-o} \approx 18$ Hz for non-adjusted and adjusted helices [13], respectively, indicates that $\Delta\chi_{\perp}^{adjusted} / \Delta\chi_{\perp}^{non-adjusted} \approx 3.6$. The detailed theoretical study of the apparent polarization of superparamagnetic helical nanomotors will be a subject of our future work.

Acknowledgement

The authors would like to thank Christian Peters and Kathrin Peyer for providing details of their experiments. This work was partially supported by the Japan Technion Society Research Fund (A.M.L.) and by the Israel Ministry for Immigrant Absorption (K.I.M.).

Appendix A: Rotation matrix

We use the definition of the three Euler angles φ , θ and ψ following Ref. [22]. The components of any vector \mathbf{W} in the body-fixed coordinate system (BCS) and in the laboratory coordinate system (LCS) are determined from the relation $\mathbf{W}^{BCS} = \mathbf{R} \cdot \mathbf{W}$, where \mathbf{R} is the rotation matrix. The rotation matrix is ex-

pressed explicitly via the Euler angles [21]

$$\mathbf{R} = \begin{pmatrix} c_\varphi c_\psi - s_\varphi s_\psi c_\theta & s_\varphi c_\psi + c_\varphi s_\psi c_\theta & s_\psi s_\theta \\ -c_\varphi s_\psi - s_\varphi c_\psi c_\theta & -s_\varphi s_\psi + c_\varphi c_\psi c_\theta & c_\psi s_\theta \\ s_\varphi s_\theta & -c_\varphi s_\theta & c_\theta \end{pmatrix},$$

where we use the compact notation, $s_\psi = \sin \psi$, $c_\theta = \cos \theta$, etc.

Appendix B: Rotational viscous resistance coefficients of a helix

We approximate the rotational viscous resistance coefficients of a helix by the corresponding values for a spheroid enclosing the helix. Let a and b be, correspondingly, the longitudinal (along the symmetry axis) and transversal semi-axes of the spheroid. The respective viscous resistances due to rotation around the symmetry axis and in perpendicular direction read [31]

$$\kappa_{\parallel} = 2\eta V n_{\perp}^{-1}, \quad \kappa_{\perp} = 2\eta V \frac{a^2 + b^2}{a^2 n_{\parallel} + b^2 n_{\perp}}, \quad (27)$$

where η is the dynamic viscosity of the liquid, V is the spheroid volume, n_{\parallel} and $n_{\perp} = (1 - n_{\parallel})/2$ are the

depolarizing factors of the spheroid. For the prolate spheroid with $a > b$ and eccentricity $e = \sqrt{1 - b^2/a^2}$ the depolarizing factor along the symmetry axis reads [25]

$$n_{\parallel} = \frac{1 - e^2}{e^3} \left(\frac{1}{2} \ln \frac{1 + e}{1 - e} - e \right). \quad (28)$$

Appendix C: Demagnetizing factors of infinitely long elliptic cylinder

The demagnetizing factor N of infinitely long elliptic cylinder with the cross-section with corresponding semi-axes \mathbf{a} and \mathbf{b} has been found in Ref. [32]:

$$N = (2\pi)^{-1} \left[4 \arctan \frac{\mathbf{a}}{\mathbf{b}} + \frac{2\mathbf{b}}{\mathbf{a}} \ln \frac{\mathbf{b}}{\mathbf{a}} + \left(\frac{\mathbf{a}}{\mathbf{b}} - \frac{\mathbf{b}}{\mathbf{a}} \right) \ln \left(1 + \frac{\mathbf{b}^2}{\mathbf{a}^2} \right) \right].$$

At $\mathbf{a} > \mathbf{b}$ it determines the demagnetization factor N_1 along the short axes. The demagnetizing factor N_2 can be found either by the permutation $\mathbf{a} \leftrightarrow \mathbf{b}$ or from the equality $N_1 + N_2 = 1$. For the regular helix with circular cross-section $N_1 = N_2 = 1/2$.

-
- [1] J. Wang, *Nanomachines: Fundamentals and Applications*, Wiley-VCH, 2013.
- [2] A. Ghosh and P. Fischer, *Nano Lett.*, **9**, 2009, 2243–2245.
- [3] L. Zhang, J. J. Abbott, L. Dong, B. E. Kratochvil, D. Bell and B. J. Nelson, *Appl. Phys. Lett.*, 2009, **94**.
- [4] L. Zhang, J. J. Abbott, L. X. Dong, K. E. Peyer, B. E. Kratochvil, H. X. Zhang, C. Bergeles and B. J. Nelson, *Nano Lett.*, 2009, **9**, 3663–3667.
- [5] A. S. Lübke, C. Alexiou, and C. Bergemann, *J. Surgical Res.*, 2001 **95**, 200–206.
- [6] S. Tottori, L. Zhang, F. Qiu, K. K. Krawczyk, A. Franco-Obregon and B. J. Nelson, *Adv. Mater.*, 2012, **22**, 811–816.
- [7] A. Ghosh, D. Paria, H. J. Singh, P. L. Venugopalan and A. Ghosh, *Phys. Rev. E*, 2012, **86**, 031401.
- [8] K. E. Peyer, F. Qiu, L. Zhang and B. J. Nelson, *IEEE International Conference on Intelligent Robots and Systems*, 2012, art. no. **6386096**, 2553–2558.
- [9] A. Ghosh, P. Mandal, S. Karmakar and A. Ghosh, *Phys. Chem. Chem. Phys.*, 2013, **15**, 10817–10823.
- [10] M. Suter, *Photopatternable superparamagnetic nanocomposite for the fabrication of microstructures*, PhD Thesis, ETH Zurich, 2012.
- [11] M. Suter, L. Zang, E. C. Siringil, C. Peters, T. Luehmann, O. Ergeneman, K. E. Peyer B. J. Nelson, C. Hierold, *Biomed. Microdevices*, 2013, **15**, 997–1003.
- [12] K. E. Peyer, E. C. Siringil, L. Zhang, M. Suter, and B. J. Nelson, *Bacteria-Inspired Magnetic Polymer Composite Microrobots*. In: Living Machines. Lepora et al. (Eds.), LNAI 8064, pp. 216227, 2013. Springer-Verlag. Berlin. 2013. P. 216-227.
- [13] C. Peters, O. Ergeneman, B. J. Nelson, C. Hierold, *Superparamagnetic Swimming Microrobots with Adjusted Magnetic Anisotropy*. In: Proc. IEEE Int. Conf. Micro Electro Mechanical Systems, Taipei, Taiwan, 2013, P. 564-567.
- [14] E. E. Keaveny, S. W. Walker and M. J. Shelley, *Nano Lett.*, 2013, **13**, 531–537.
- [15] Man, Y. and E. Lauga, The wobbling-to-swimming transition of rotated helices, *Phys. Fluids* 25, 071904 (2013).
- [16] Gjolberg, E. N., Investigation of Artificial Bacterial Flagella Propulsion, Master Thesis, Institute of Robotics and Intelligent Systems, ETH Zurich, CH-8092, Zurich Switzerland, 2012.
- [17] K. I. Morozov, A. M. Leshansky, *Nanoscale*, 2014, **6**, 1580-1588.
- [18] P. G. de Gennes, J. Prost *The Physics of Liquid Crystals*, 2nd ed., Clarendon Press, Oxford, 1993.
- [19] J. Happel and H. Brenner, *Low Reynolds Number Hydrodynamics*, Kluwer, 1983.
- [20] Generally, the principal rotation axis of a helix slightly deviates from x_3 , however, this misalignment has a negligible effect on the dynamics and can be ig-

- nored [17].
- [21] J. Diebel, *Representing Attitude: Euler Angles, Unit Quaternions, and Rotation Vectors*, Matrix, Citeseer, 2006.
 - [22] L. D. Landau and E. M. Lifshitz, *Mechanics*, 3rd ed., Pergamon Press, Oxford, 1976.
 - [23] C. Caroli and P. Pincus, *Phys. kondens. Materie*, 1969, **9**, 311–319.
 - [24] A. Cēbers and M. Ozols, *Phys. Rev. E*, 2006, **73**, 021505.
 - [25] L. D. Landau, E. M. Lifshitz, *Electrodynamics of Continuous Media*, 2nd ed.; Pergamon Press, Oxford, 1984.
 - [26] R. M. Erb, R. Libanori, N. Rothfuchs, A. R. Studart, *Science*, 2012, **335**, 199–204.
 - [27] A. F. da Fonseca, C. P. Malta, D. S. Galvao, *Nanotechnology* 2006, **17**, 5620–5626.
 - [28] R. E. Rosensweig, *Ferrohydrodynamics*, Cambridge University Press, Cambridge, 1985.
 - [29] K. E. Peyer, L. Zhang, and B. J. Nelson, *Nanoscale*, 2013, **5**, 1259–1272.
 - [30] M. Suter, O. Ergeneman, J. Zürcher, S. Schmid, A. Camenzind, B. J. Nelson, C. Hierold, *J. Micromech. Microeng.*, 2011, **21**, 025023.
 - [31] Jeffrey, G. B. The motion of ellipsoidal particles immersed in a viscous fluid. *Proc. R. Soc. London A* **1922**, *102*, 161–179.
 - [32] W. F. Brown, Jr., *Magnetostatic Principles in Ferromagnetism*, North-Holland, Amsterdam, 1962.